



ORIGINAL RESEARCH ARTICLE

Tensile and Low Cycle Fatigue Response of SS321 at Room Temperature

Aakash, S.C.S.P. Kumar Krovvidi, G.V. Prasad Reddy, R. Kannan, S. Arun Kumar, S. Mahadevan, A. Nagesha, and A.K. Dureja

Submitted: 19 December 2023 / Revised: 5 April 2024 / Accepted: 13 May 2024

SS321 is a titanium-stabilized steel of the SS304 class of steels and is a candidate material for bellows. The present study deals with the tensile and low cycle fatigue (LCF) behavior of the steel at room temperature. The curve fitting of the true stress and true plastic strain data was found to follow the Ludwigson equation. From the cyclic stress response, the material was found to exhibit secondary hardening due to the formation of strain-induced martensite, which was quantified through x-ray diffraction. The LCF properties generated were used for establishing the isotropic and kinematic hardening parameters of the material, and the same were validated based on the satisfactory prediction of the cyclic stress–strain hysteresis loops using nonlinear finite element analysis.

Keywords bellows, combined nonlinear isotropic-kinematic hardening, FE analysis, low cycle fatigue, SS321, tensile

1. Introduction

Steels belonging to SS304 family of austenitic stainless steels (ASSs) are widely used for the manufacture of pressure vessels and piping system components operating below the creep range of the material (475 °C). ASS is prone to sensitization with an attendant problem of intergranular stress corrosion cracking during welding or in service above 550 °C. The problem is generally addressed by lowering the carbon content or through the addition of stabilizers such as Nb or Ti to the steel (Ref 1). SS321 is a titanium-stabilized form of SS304 steel, which possesses a higher strength compared to that of the low carbon version (i.e., SS304L). SS321 steel is one of the candidate materials for the bellows in the bellow-sealed valves in light water nuclear power reactors (Fig. 1).

As bellows are manufactured by forming operation, material properties such as uniform elongation, yield strength (YS), ultimate tensile strength (UTS) and the plastic flow response of the material are important (Ref 2). Bellows in critical systems such as those in nuclear power plants need to be designed in compliance with the design codes such as ASME boiler and pressure vessel code/section-III or RCC-MR. The design as per the codes follows “design by analysis”, which requires the data such as the design fatigue curve, cyclic stress–strain curve and

the constitutive parameters predicting the isotropic/kinematic hardening of the material (Ref 3).

The family of SS304 steels is known to yield strain-induced martensite (SIM) under tensile and low cycle fatigue (LCF) loading at room temperature (Ref 4). The occurrence of dynamic strain aging (DSA) under tensile loading of SS304L in the temperature range of 400–700 °C was also reported (Ref 5). Further, the tensile flow curve of SS304 has been found to follow the Ludwigson fit (Ref 6) at room temperature. Under strain-controlled cyclic loading, the SS321 is reported to exhibit an initial hardening followed by cyclic saturation and secondary hardening, before the sudden drop in stress due to crack propagation (Ref 7). Studies on SS321 exposed to cyclic loading have also reported the formation of SIM using in situ neutron diffraction stress analysis (Ref 8). Formation of SIM in LCF loading at various temperatures in the range of 30 to 260 °C was also reported (Ref 9). It was observed that SIM formation reduces exponentially with increase in temperature and there was no significant effect of the strain rate on the SIM formed during LCF testing (Ref 10).

The present investigation deals with the tensile and LCF response of SS321 steel at room temperature. The motive of this work is to generate the constitutive parameters defining the isotropic and kinematic hardening of the material and thereby predict the cyclic stress–strain behavior under LCF loading through nonlinear inelastic finite element (FE) analysis of the SS321 bellows.

2. Experimental

The specimens for this investigation were extracted from a 25-mm thick plate conforming to ASTM A240 (Ref 11). The chemical composition of the material established using wet chemical analysis is given in Table 1. Initially, the material was solution-annealed at 1050 °C for 1 h followed by water quenching. Specimen for optical microscopy was extracted, polished and etched electrolytically using 10% oxalic acid at 2 V.

Aakash and A.K. Dureja, Homi Bhabha National Institute, Mumbai 400094, India; and Bhabha Atomic Research Centre, Mumbai 400085, India; S.C.S.P. Kumar Krovvidi, R. Kannan, and S. Arun Kumar, Indira Gandhi Centre for Atomic Research, Kalpakkam 603102, India; and G.V. Prasad Reddy, S. Mahadevan, and A. Nagesha, Indira Gandhi Centre for Atomic Research, Kalpakkam 603102, India; and Homi Bhabha National Institute, Kalpakkam 603102, India. Contact e-mail: aakashchahal@gmail.com.

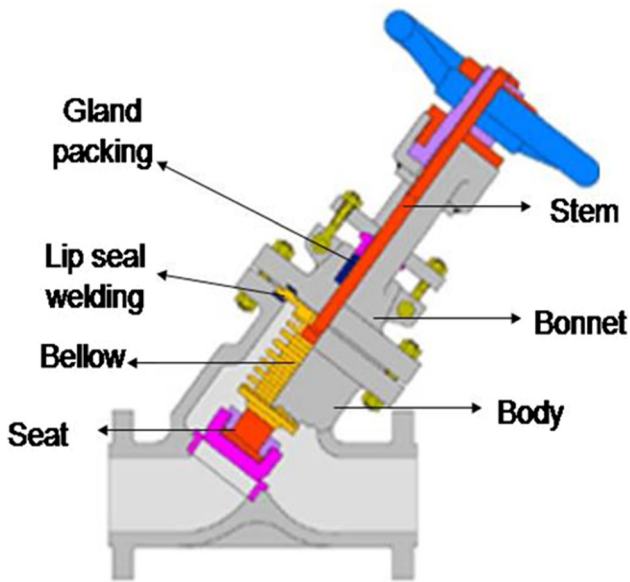


Fig. 1 Schematic of the bellows in bellow-sealed valves

The tensile tests were conducted on a Hung-Ta tensile testing system (Fig. 2a) using specimens of 25-mm gauge length and 5-mm gauge diameter (Fig. 2b) and conforming to ASTM E8/8 M (Ref 12). The Ferrite number (FN) for the tensile tested specimen was measured using Fischer feritscope before and after testing. Fully reversed axial strain-controlled LCF tests were carried out at different total strain amplitudes ranging from ± 0.25 , ± 0.4 , ± 0.5 , ± 0.6 and $\pm 0.8\%$ on specimens with 10-mm gauge diameter and 25-mm gauge length conforming to ASTM E606/606 M-21 (Fig. 3) (Ref 13) on a BISS servo-electric fatigue testing system. Both the tensile

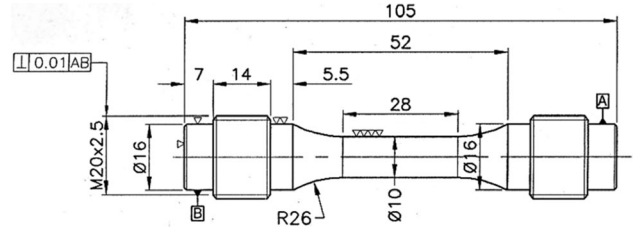


Fig. 3 The specimen geometry used for LCF testing (dimensions in mm)

Table 1 Chemical composition of SS321 (wt.%)

Element	C	Cr	Ni	Ti	Mn	S	P	Si	N
Measured	0.055	17.5	10	0.57	1.8	0.012	0.01	0.55	0.03
As per ASTM A240 UNS32100	< 0.08	17-19	9-12	5(C + N) / 0.7% (Max)	< 2	< 0.03	< 0.04	< 0.75	< 0.1

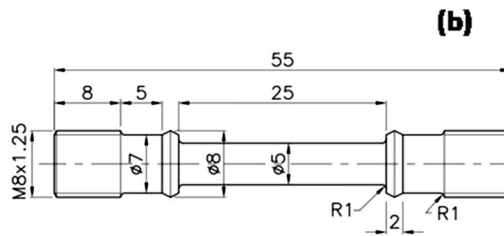


Fig. 2 Tensile testing of SS321: (a) HungTa tensile testing machine and (b) schematic of the tensile specimen (dimensions in mm)

and LCF tests were carried out at room temperature at a strain rate of $3 \times 10^{-3} \text{ s}^{-1}$. The number of cycles to failure in LCF tests (N_f) are given by the cycle in which the peak tensile stress drops by 40% of that of saturated / half-life cycle. Further, the specimens were separated into two parts by application of tensile (pull) loading.

Measurement of martensite volume fractions was carried out using Proto iXRD residual stress analyzer instrument using x-ray diffraction (XRD) technique as per the ASTM-E975-22 (Ref 14). The two diffraction peaks, (220) & (200) corresponding to the fcc (γ) phase, and two diffraction peaks, (211) & (200) for the bcc (α) phase, were recorded using Cr- K_α radiation. The volume fraction of austenite was estimated at discrete locations on the fractured LCF specimens in the shoulder and gauge regions. On each of the strain amplitude specimens (ranging from ± 0.25 to $\pm 0.8\%$), the XRD mea-

surements were carried out along two diametrically opposite locations identified as 0° and 180° along the gauge length. A 2-mm circular aperture with 5° beta oscillation was used for the collection of the XRD patterns in the angular range of 70° to 170° . The volume fraction of austenite was estimated after necessary background correction, using suitable peak fitting algorithms available in the XRDWIN 2.0 software. The volume fraction of martensite is subsequently evaluated. The procedure

Table 2 Tensile properties of SS321 at room temperature

Parameter	0.2% YS, MPa	UTS, MPa	%Elongation at fracture
Value	243	601	62

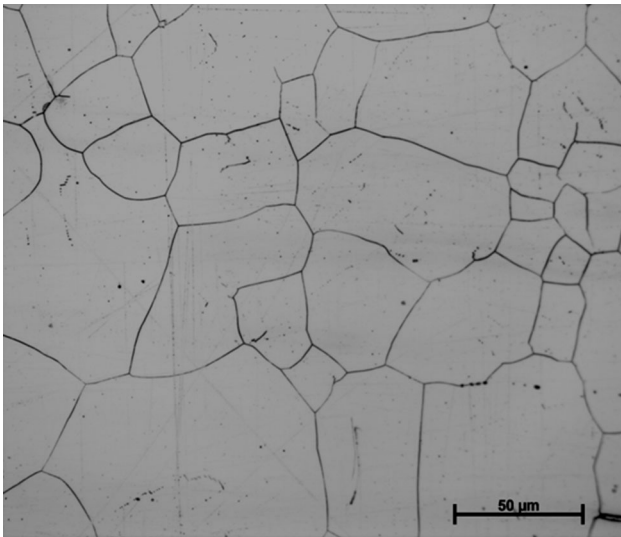


Fig. 4 Microstructure of SS321

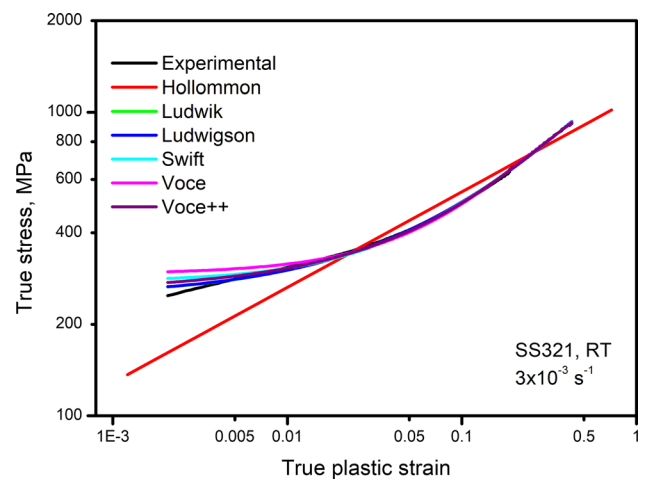


Fig. 6 Plastic flow response of the SS 321 under tensile loading

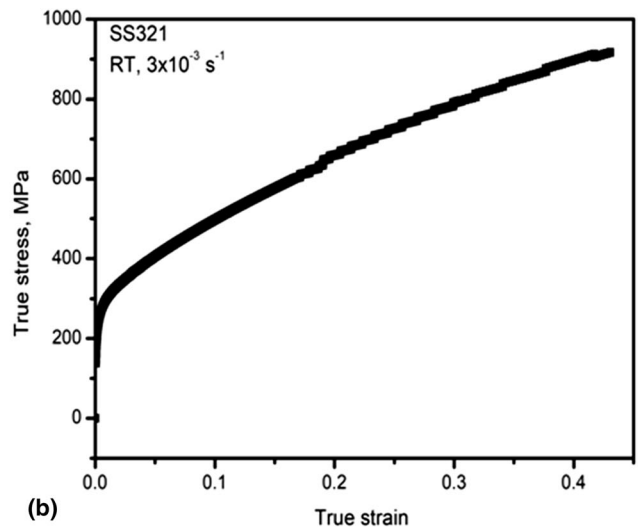
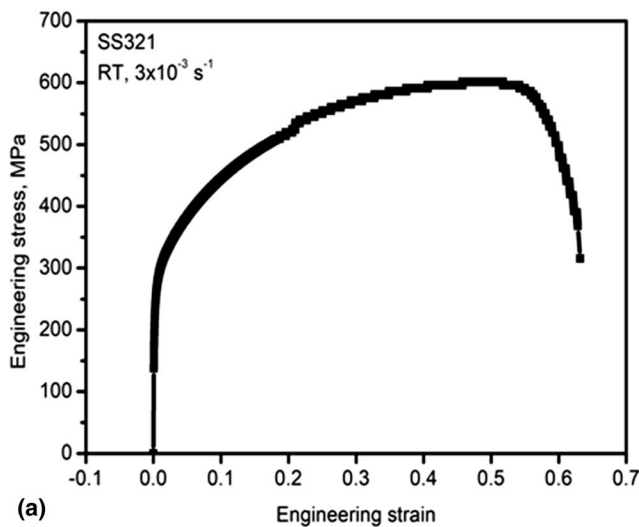


Fig. 5 (a) Engineering stress–strain curve and (b) true stress–strain curve of SS321 at room temperature

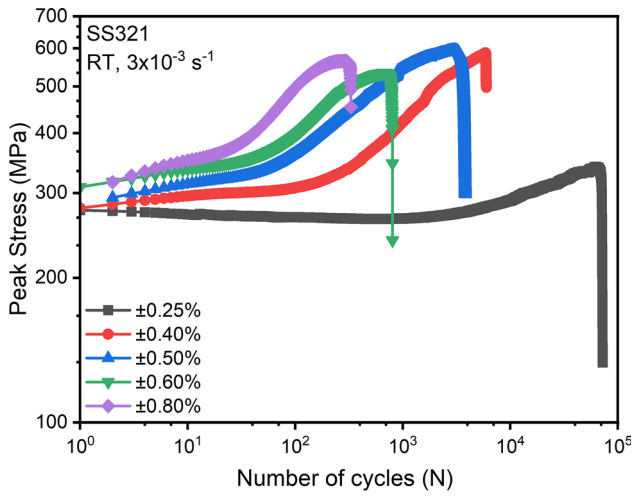


Fig. 7 Cyclic stress response of SS321 at various strain amplitudes

Table 3 The values of χ^2 for different constitutive equations

Flow curve Fit	Hollomon	Ludwik	Swift	Ludwigson	Voce	Voce++
χ^2	3001	24.2	24.6	10.1	36	16

was validated and calibrated using known standard with RA 10.4%.

3. Results

3.1 Chemical Composition and Microstructure

The chemical composition of SS321 (Table 1) shows that the material conforms to ASTM A240, UNS321000 (Ref 11). The microstructure of the material showed a polycrystalline structure with an average grain size of 50 μm as presented in Fig. 4.

3.2 Tensile Response

The engineering and true stress–strain curves of SS321 are shown in Fig. 5(a) and (b), respectively. The YS, UTS and % elongation (% El) of the material at the testing conditions are listed in Table 2. The FN of the material is found to be in the range 0.27–1.0 in the untested condition, but the same is found to increase upon loading. An average value of 40 ± 1 FN was noted along the gauge length of the tensile tested sample with a peak observed at 60 ± 5 FN in the vicinity of the fracture surface.

The tensile response of the material in the plastic range is presented in Fig. 6. The experimentally obtained plastic flow response under tensile loading is analyzed using Hollomon, Ludwik, Ludwigson, Swift and Voce equations (Ref 15) as given below:

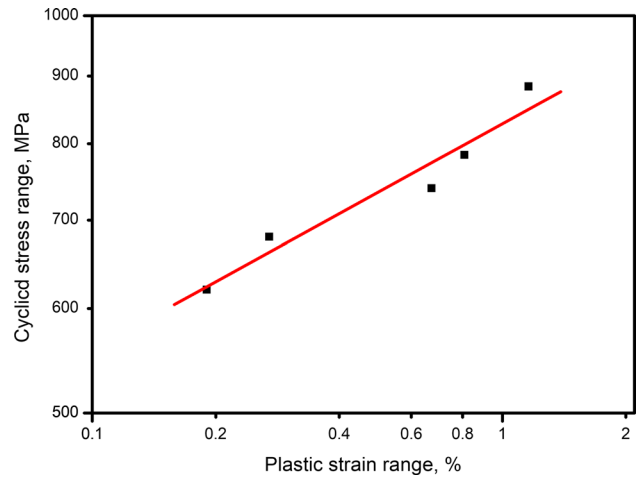


Fig. 8 Cyclic stress–strain curve in plastic range

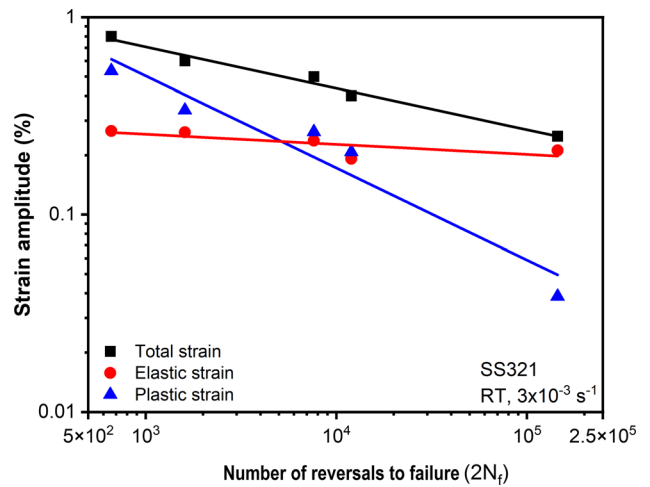


Fig. 9 Variation of cyclic life with strain amplitude

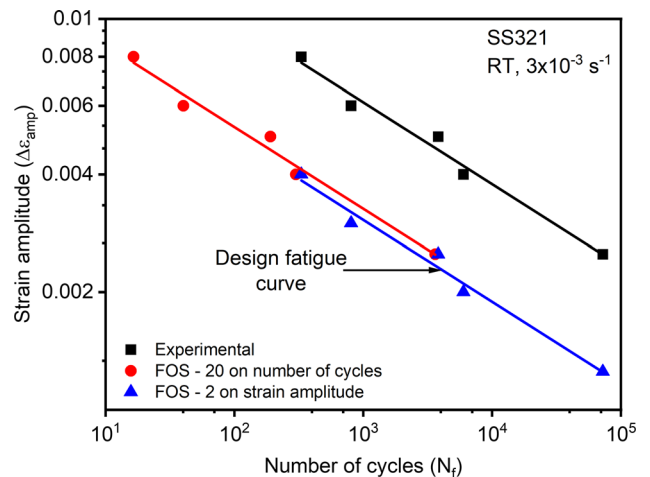


Fig. 10 Design fatigue curve of SS321 at room temperature

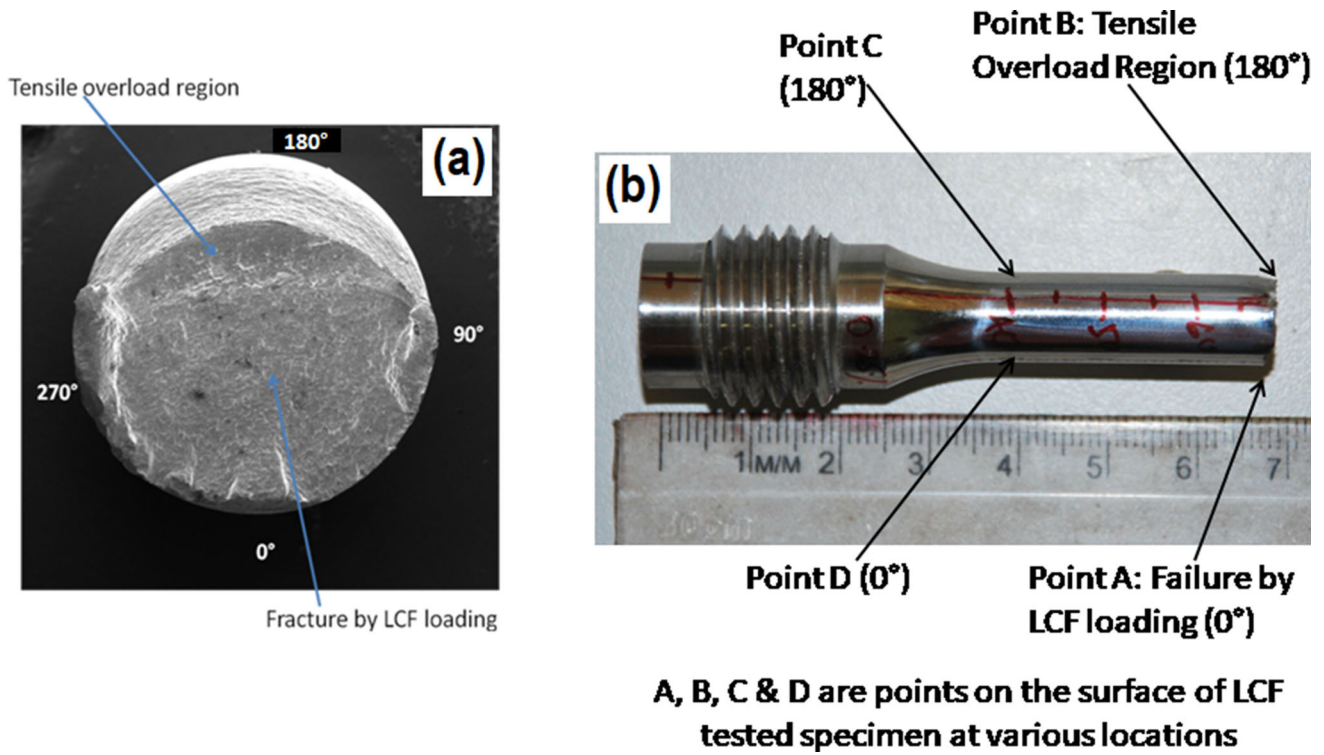


Fig. 11 (a) Circumferential orientations and (b) position along the gauge length for a typical LCF-tested specimens

(i) Hollomon equation:

$$\sigma = K_H \epsilon_p^{n_H} \quad (\text{Eq 1})$$

where σ is true stress and ϵ_p is true plastic strain. K_H is the strength coefficient and n_H is the strain-hardening exponent.

(ii) Ludwik equation:

$$\sigma = \sigma_o + K_L \epsilon_p^{n_L} \quad (\text{Eq 2})$$

where K_L is the strength coefficient, n_L is the strain-hardening exponent and σ_o is the yield strength of the material.

(iii) Ludwigs equation:

$$\sigma = K_1 \epsilon^{n_1} + \exp(K_2 + n_2 \epsilon) \quad (\text{Eq 3})$$

where K_1 is the strength coefficient and n_1 is the strain-hardening exponent. The second term accounts for the deviation of the flow curve from the exponential fit (predicted by the Hollomon relationship). K_2 and n_2 are curve-fitting constants.

(iv) Swift equation:

$$\sigma = K_S (\epsilon_o + \epsilon_p)^{n_S} \quad (\text{Eq 4})$$

where K_S is the strength coefficient, ϵ_o is the pre-strain in the material and n_S is the strain-hardening exponent.

(v) Voce equation:

$$\sigma = \sigma_S - (\sigma_S - \sigma_I) \exp(-n_V \epsilon_p) \quad (\text{Eq 5})$$

where σ_S is the saturation stress. σ_I initial stress and n_V defines the rate at which flow stress varies from initial stress to saturation stress.

Voce equation is further modified to (Voce++ equation) by adding a quadratic root term and a linear term for better prediction of the the rising rate of flow stress as given in Eq 6.

$$\sigma = \sigma_S - (\sigma_S - \sigma_I) \exp(-n_V \epsilon_p) + n_1 \sqrt{\epsilon_p} + n_2 \epsilon_p \quad (\text{Eq 6})$$

It can be seen from Table 3 that by addition of the two terms, quadratic root and the linear terms to voce model improved the prediction (χ^2 value reduced to 16 from 30). However, the Ludwigs fit is found to predict the experimental results more closely with a χ^2 value of 10.1 as shown in Table 3.

3.3 LCF Response

The cyclic stress response (CSR) of the material is given in Fig. 7. The cyclic stress response of the material shows initial hardening, followed by hardening at a lesser rate and a secondary hardening at a higher rate. The secondary hardening is attributed to strain-induced martensite as discussed in the subsequent section. At strain amplitude of $\pm 0.25\%$, after initial hardening, the material showed almost saturation till the start of the secondary hardening beyond 10^4 cycles.

The cyclic stress-strain curve (CSSC) of the material was generated from the stable hysteresis loops at various strain amplitudes, and the same is shown in Fig. 8. The stress-strain relationship corresponding to the CSSC is generally represented in the form of following equation (Eq 7) given in RCC-MR (Ref 16). The first part in the equation represents the elastic strain range and the second part, the plastic strain range. In the plastic range, the cyclic stress strain curve is generated by

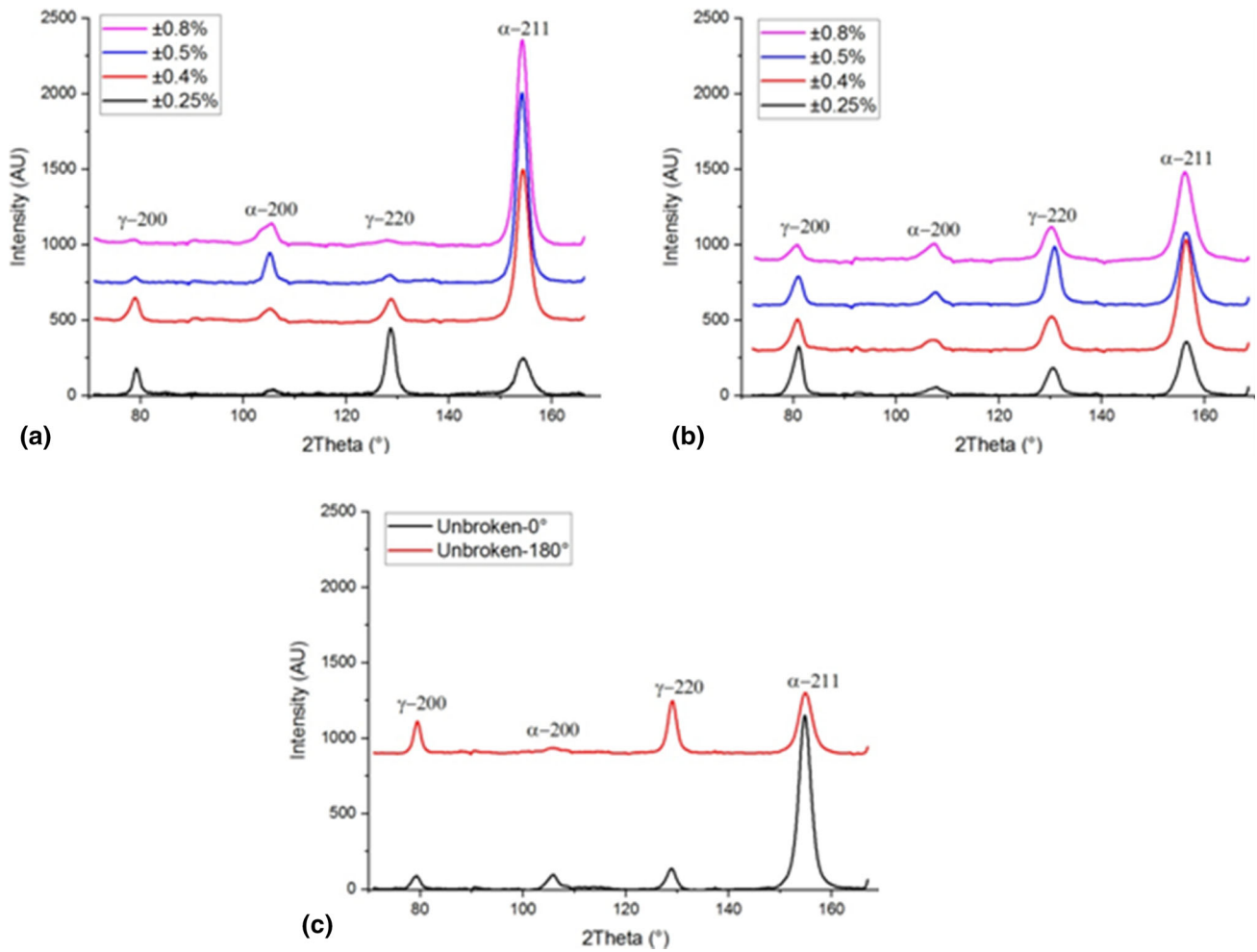


Fig. 12 XRD patterns of the LCF tested specimens: (a) at 0° orientation (failure by LCF loading), (b) 180° orientation (subjected to tensile pull) and (c) Unbroken specimen tested at ± 0.4% strain amplitude upto initiation of the load fall (beginning of crack propagation).

plotting the stress range in the stable hysteresis loops with plastic strain range (%) as shown in Fig. 8.

$$\overline{\Delta \varepsilon}_t(\%) = 100 \cdot \frac{2(1+\nu)}{3E} (\overline{\Delta \sigma}) + \left(\frac{\overline{\Delta \sigma}}{K} \right)^{1/m} \quad (\text{Eq 7})$$

The strain-life relationships in terms of elastic, plastic and total strains are given in Fig. 9. The design fatigue curves are constructed from the experimental best-fit strain-life plots by applying a factor of safety (FOS) of 2 on the strain range or a factor of 20 on the number of cycles to failure, considering the more conservative value at each point (Ref 17). The design fatigue curve generated for SS321 at room temperature by incorporating the abovementioned FOS is presented in Fig. 10.

The LCF testing of the specimens was terminated when the load drops by 40% in the cyclic stress response curve. Further, the specimen was separated into two parts by tensile pull. Azimuthally, the orientation of the specimens was marked such that 0° corresponds to the region failed by LCF loading and 180° corresponds to the region failed by tensile loading as shown in Fig. 11(a). In all the specimens, the gauge length starts at 40 mm and the fracture surface located between 60-65 mm and for reference, points A, B, C and D were defined on

the surface of the longest part of the specimen as shown in Fig. 11(b).

3.4 Estimation of Volume Fractions by XRD

Typical XRD patterns (as per the ASTM-E975-03) obtained after LCF testing at strain amplitudes of ± 0.25, ± 0.4, ± 0.5 and ± 0.8%, obtained at 0° and 180° orientations are presented in Fig. 12(a) and (b), respectively. To study the effect of the tensile deformation on SIM, XRD investigation was carried out on the LCF-tested specimen before tensile pull. The specimen was tested upto initiation of the load fall (beginning of crack propagation). The XRD patterns on the specimen subjected to pure LCF loading (without the tensile pull) is given in Fig. 12(c). The volume fraction of austenite phase (V_γ) was determined by direct comparison of integrated intensities of XRD peaks of the austenite phase (I_γ) to that of ferritic/martensitic phase (I_x) with theoretical intensities. For brevity, the austenite volume fraction can be determined by (Ref 18):

$$\% \text{ of Austenite} = (V_\gamma)100 = \left(\frac{\frac{I_\gamma}{R_\gamma}}{\frac{I_\gamma}{R_\gamma} + \frac{I_x}{R_x}} \right) 100 \quad (\text{Eq 8})$$

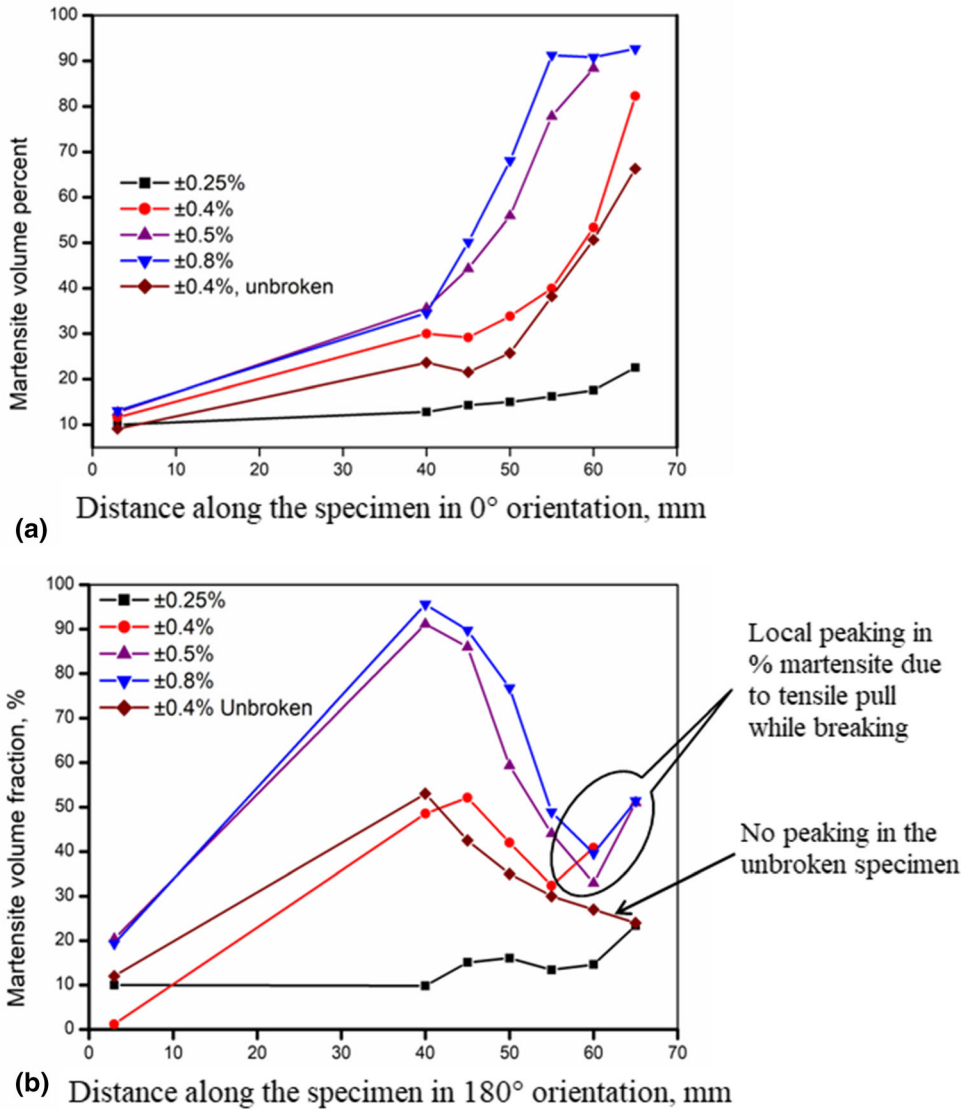
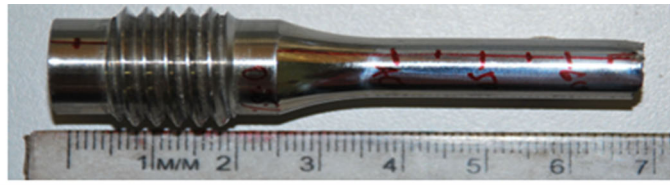


Fig. 13 SIM along the gauge length at (a) 0° and (b) 180° orientations

where R_γ and R_α are the scaling factors corresponding to the austenite and ferritic/martensitic phases, respectively. The above factors include the terms corresponding to structure, temperature, volume of unit cell, multiplicity of the lines and the polarization correction. The martensite fraction is evaluated from

$$\% \text{ of Martensite} = 100 - \% \text{ of Austenite} \quad (\text{Eq 9})$$

The variation of the SIM fraction measured along the gauge length of the specimens (from one end till fracture surface) tested at ± 0.25 , ± 0.4 , ± 0.5 , $\pm 0.8\%$ and unbroken specimen tested at $\pm 0.4\%$ (specimen with fatigue crack but not separated to two parts by tensile pull) in 0° and 180° orientations is given in Fig. 13(a) and (b), respectively.

Formation of strain-induced martensite (SIM) along the gauge length portions of the tested specimens is evident from Fig. 13(a) and (b). For the surface at the 0° orientation, it is observed that the fraction of SIM increases in the gauge region

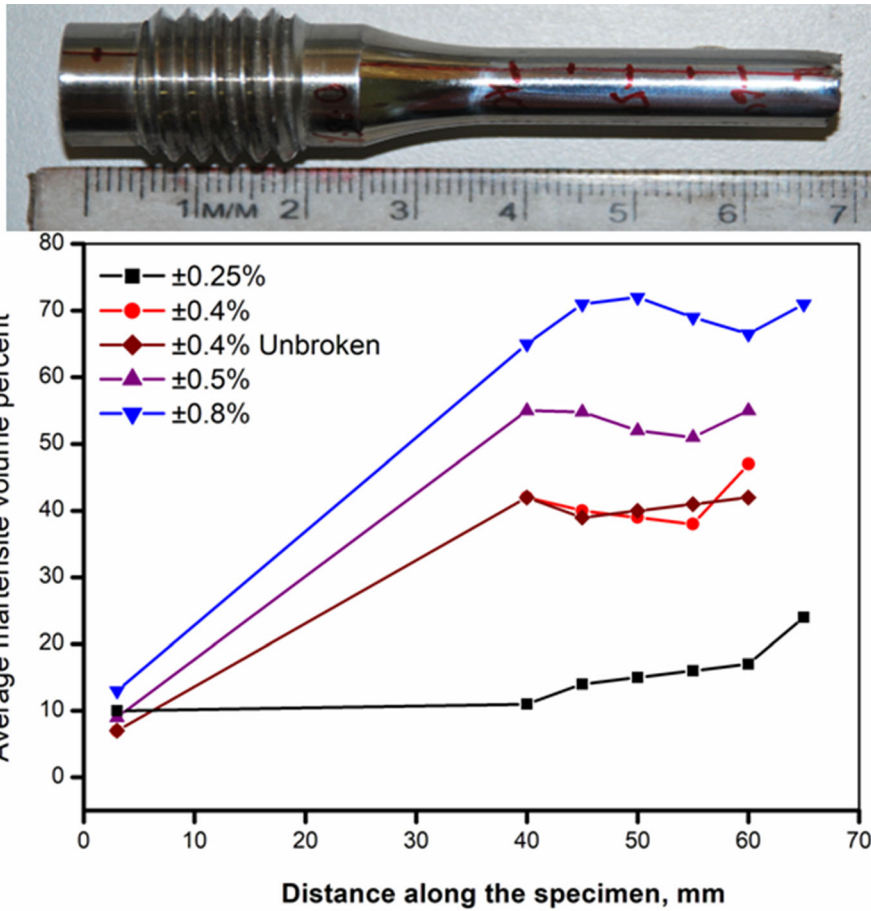


Fig. 14 Average values of SIM along the gauge length

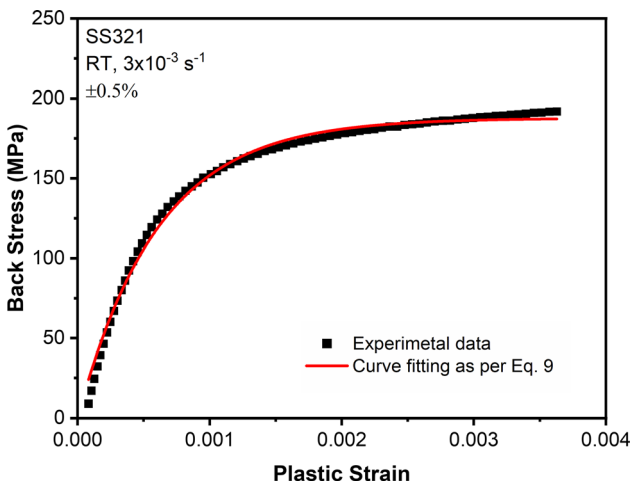


Fig. 15 Variation of back stress with plastic strain for SS321 at RT in the region of hardening

toward the fracture surface. Concentration of deformation in the vicinity of the primary fatigue crack is reflected in the form of peaks in the amount of SIM formed at the above locations. Further, it was also observed that the % of SIM is increasing with increase in the strain amplitude employed during LCF

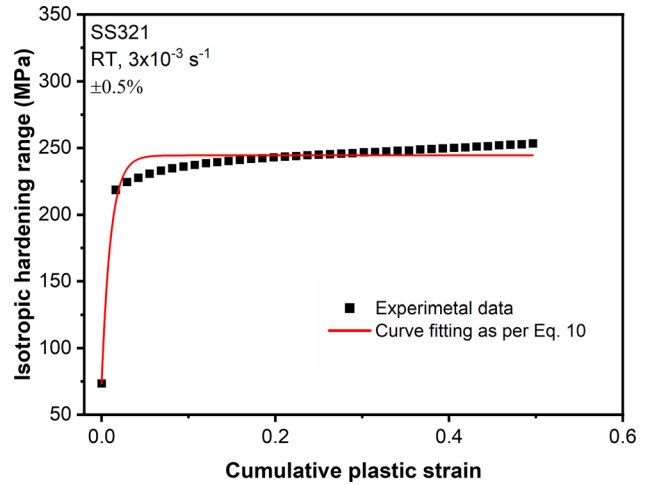


Fig. 16 Variation of range of isotropic hardening with cumulative plastic strain for SS321 at RT in the region of hardening

testing. The average value of the SIM along the gauge length specimen is given in Fig. 14. It can be seen from the averaged SIM plot that the SIM in the gauge length region is almost constant.

4. Parameters for Nonlinear Isotropic–Kinematic Hardening Model

4.1 Estimation of Parameters

The von-Mises yield function (f) of the nonlinear combined isotropic–kinematic hardening model employed for the FE analysis performed using ABAQUS is represented by:

$$f = \left(\frac{3}{2} (\sigma' - x') : (\sigma' - x') \right)^{1/2} - r - \sigma_y = 0 \quad (\text{Eq 10})$$

where σ' , x' , r and σ_y are the deviatoric stress tensor, deviatoric back stress tensor, isotropic hardening function and yield stress of the material, respectively (Ref 19).

In the case of nonlinear kinematic hardening, the back stress is defined by the following expression:

$$\dot{x} = \frac{2}{3} c \dot{\epsilon}^p - \gamma x \dot{p} \quad (\text{Eq 11})$$

where x is the back stress, $\dot{\epsilon}^p$ and \dot{p} are the plastic strain rate and effective plastic strain rate; c and γ are the kinematic hardening material constants. The constant γ determines the rate of saturation of stress and $\frac{c}{\gamma}$ determines the magnitude of saturation.

In the case of isotropic hardening, the isotropic function (r) is defined by the following equation,

$$\dot{r} = b(Q - r)\dot{p} \quad (\text{Eq 12})$$

Here, b and Q are material constants, which give an exponential shape to the stress–strain response which saturates with increasing plastic strain (Ref 20, 21). (The constitutive model deals with time-independent plasticity and the rate terms in the equations given in 11 & 12 consist of pseudo-time step.) The variation of the back stress with the plastic strain is presented in Fig. 15. The parameters c and γ were estimated to be 180000 and 840, respectively. The isotropic hardening parameters b and Q are estimated by curve fitting of the plot between the isotropic hardening range with the equivalent plastic range. The values of Q and b are found to be 170 and 11, respectively (Fig. 16). The values of the constitutive parameters of the model are given in Table 4.

4.2 Validation of the Constitutive Parameters

The constitutive parameters estimated in section 4.1 were validated by predicting the hysteresis loops at the strain amplitudes of ± 0.6 and $\pm 0.8\%$ using finite element (FE) analysis. The geometry of the LCF specimen was modeled in ABAQUS with a single 4-noded axisymmetric shell element (CAX4R). As the loading applied is pure axial displacement, a gauge length of 5 mm was modeled with the applied displacements also corrected proportionately. The specimen is modeled with a single axisymmetric element. Hence, the size of the element is 5×5 mm. For a 5-mm gauge length, the displacement corresponding to the strain amplitude of $\pm 0.6\%$ is ± 0.03 mm and the same for $\pm 0.8\%$ is ± 0.04 mm. Corresponding displacements were applied so that the strain in the element is ± 0.6 and $\pm 0.4\%$. The kinematic and isotropic hardening parameters as defined in Table 4 were used for the model. The boundary conditions and applied loading are presented in Fig. 17.

Axisymmetry boundary condition was applied at the axis. The bottom face of the specimen was constrained for y -movement, and the top face was subjected to a displacement along the y -direction to simulate the axial strain applied during the fatigue testing. The numerically predicted and experimentally observed hysteresis loops of the material during first cycle for the two strain amplitudes are presented in Fig. 18(a) and (b) for the strain amplitudes of ± 0.6 and $\pm 0.8\%$, respectively.

5. Discussion

The tensile response of the material in the plastic regime exhibited serrated flow as shown in Fig. 19. Serrated or jerky flow in the plastic portions of the stress–strain plots at specific strain rate/temperature combinations in austenitic stainless steels is often associated with the occurrence of DSA. In the case of type 304 SS, the phenomenon of DSA is known to occur in the temperature domain of 250–550 °C (Ref 22). The observed jerky stress–strain response in the present case (Fig. 19) could be associated with the occurrence of strain-induced martensite transformation in the material. The same was confirmed by increase in the FN measured before and after tensile testing. The formation of strain-induced martensite in SS304 has also been reported by other investigators (Ref 23, 24).

The CSR of the material shows initial hardening, followed by hardening at a lesser rate and a secondary hardening at a higher rate (Fig. 7). Initial hardening of the material under LCF

Table 4 Constitutive parameters defining isotropic and kinematic hardening of the material

Young's Modulus, GPa	Poisson ratio, ν	σ_0 , MPa	Kinematic hardening parameters		Isotropic hardening parameters	
			c , MPa	γ	Q , MPa	b
200	0.3	74	180000	840	170	11

loading is attributed to proliferation of the dislocations. The

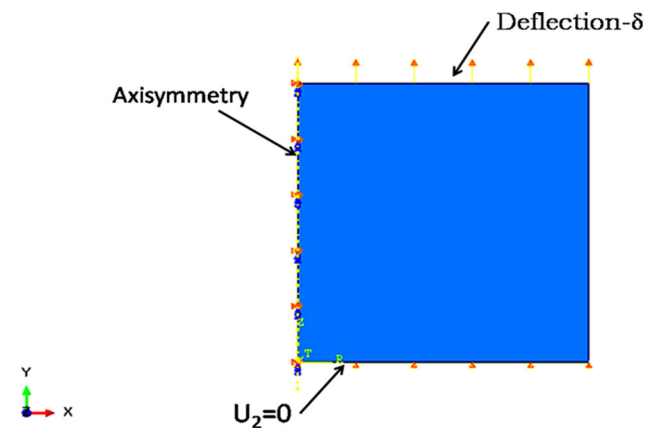


Fig. 17 Geometry and boundary conditions of the FE model

reason for the secondary hardening in the stress response was found to be strain-induced martensite transformation in the steel. The secondary hardening takes place after some incubation period which could be associated with the accumulation of plastic strain required for the SIM transformation. At lower strain amplitudes ($\pm 0.25\%$) between the initial hardening and the secondary hardening, the material exhibited marginal cyclic softening response. Similar CSR was also reported when the steel was subjected to LCF testing at different strain rates at room temperature (Ref 7). At lower strain amplitudes, after initial hardening, cyclic softening response is commonly shown in most of the austenitic stainless steels such as SS316 family of steels (Ref 25, 26). At higher strain amplitudes, the steels show saturation with a marginal cyclic hardening response. The difference in the responses of the CSR at different strain amplitudes was explained by (Ref 27), and it was indicated that the increase in strain amplitude results the transition from planar slip bands to dislocation cell or dislocation wall structure. However, secondary hardening of the SS304 family of the steels is due to SIM during cyclic loading (Ref 8–10). The presence of SIM is also observed in the LCF tested samples as shown in Figs. 13 and 14.

The SIM was found to be the maximum near fracture surface (point A at 60–65 mm position) in 0° orientation. In 180° orientation, it was found that the SIM is the maximum at the beginning of the gauge length (Point C at 40 mm position) and reduced along the gauge length. The peak in the SIM at the extremities of the gauge portion can be attributed to crack nucleation sites and strain accumulation. It should be noted that the micro-cracks which were initiated at point A (Fig. 11) propagated faster than the micro-cracks at point C. During crack propagation, the strain accumulation is maximum at the tip of the crack and minimum at the surface at the other end. The applied strain is partially absorbed by the opening/closing of the fracture surfaces, and hence, the strain experienced at point B is the minimum. Thus, strains are accumulated ahead on the crack tip rather than on the surface at point B. Hence, the contrasting trend of the SIM along the gauge length in 0° and 180° is justified. It is worth investigating the effect of the additional tensile pull on the specimens at 180° orientation at point B. However, in presence of the pre-existed fatigue crack, the specimen fractures with less plastic deformation and hence, the accumulation of the plastic deformation due to the tensile

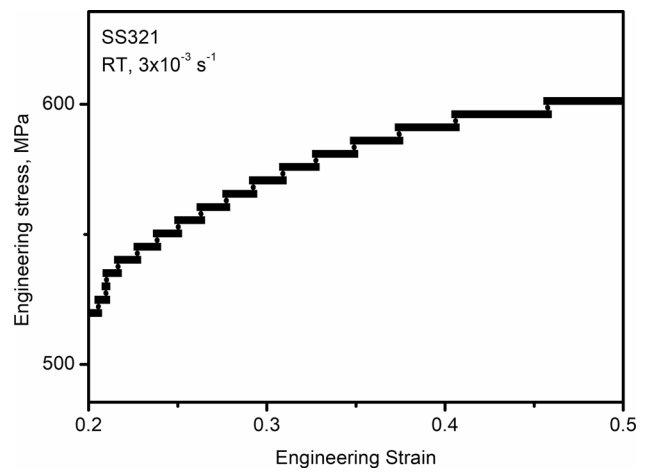


Fig. 19 Serrated plastic flow in the tensile response of the steel due to SIM

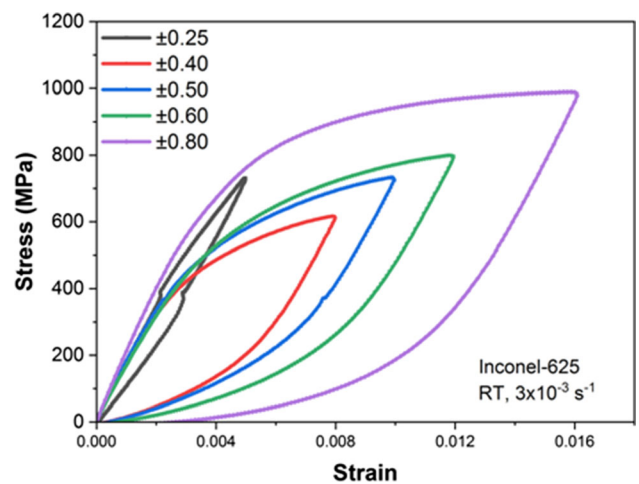


Fig. 20 Non-Masing behavior of SS321 material at room temperature (strain rate: $3 \times 10^{-3} \text{ s}^{-1}$)

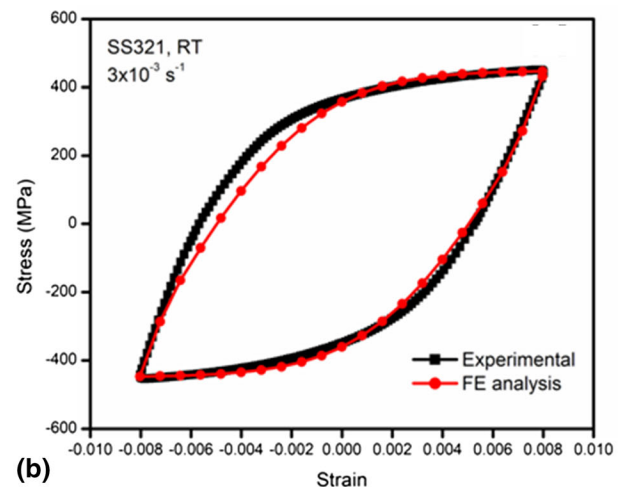
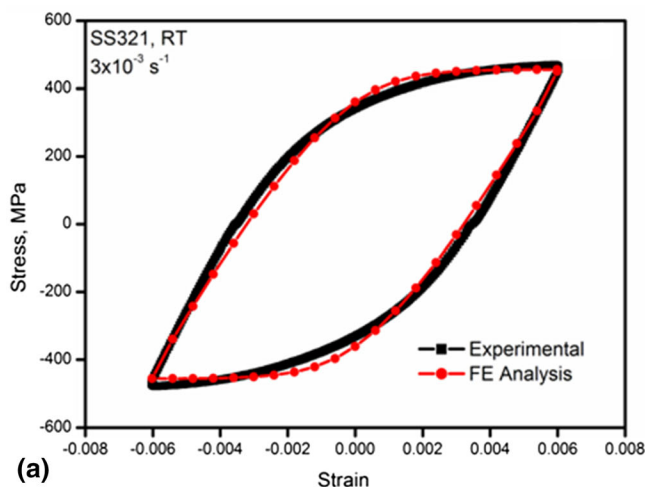


Fig. 18 Numerically predicted and experimentally observed hysteresis loops at (a) $\pm 0.6\%$ and (b) $\pm 0.8\%$

pull is less. The change in the length of the specimen at 0° to 180° is also found to be insignificant. It is also interesting to note that the SIM measured in the 0° orientation in the LCF tested specimen at ± 0.4% strain amplitude without tensile pull showed similar trend of SIM to that of the specimen subjected to LCF and tensile pull at the corresponding strain amplitude and orientation. However, the local increase in the SIM in the vicinity of the tensile pull at point B (180°, near fracture surface) marked in Fig. 13 is attributed to the tensile pull. It can be seen that the average value of the SIM along the gauge length is almost constant (Fig. 14).

Ludwik, Ludwigson and Swift's equation is found to predict the plastic flow response of the material under tensile loading with more accurate prediction results from the Ludwigson equation (Fig. 6). A similar tensile response for SS304 steels was observed by Andersson (2005) (Ref 15). A close agreement is seen between the numerically predicted and experimentally obtained hysteresis loops, as shown in Fig. 18(a) and (b). The material is found to exhibit non-Masing response (Ref 28) at a strain rate of $3 \times 10^{-3} \text{ s}^{-1}$ as shown in Fig. 20(a). It may be noted that the microstructural stability is essential for Masing behavior. With the changes in the strain amplitude, stacking fault energy (SFE), temperature and type of loading, microstructural instability takes place in materials leading to non-Masing behavior. Yadav et al., (2023) (Ref 29) reported that the strong nonlinear variation of the cyclic plastic strain energy density (CPSD—which is the area within the hysteresis loop) with the strain amplitude. Under cyclic loading, various phenomena such as phase transformation, dislocations generation, creation of stacking faults and deformation twins are responsible for the nonlinear variation of the CPSD with the strain amplitude. The minor difference between the numerically predicted and experimentally obtained hysteresis loops could be attributed to the non-Masing response of the material.

6. Conclusions

The following are major conclusions drawn from the present investigation.

1. The material was found to be exhibiting serrated plastic flow under tensile response which is attributed to the formation of strain-induced martensite.
2. Ludwigson fit was found to closely model the plastic flow behavior of the alloy under tensile loading.
3. The LCF response of the material at various strain amplitudes was studied. The strain-life relationships were plotted. Other data required for fatigue design such as cyclic stress-strain curve, design fatigue curve and constitutive parameters defining the material's cyclic hardening were estimated.
4. The material displays pronounced secondary hardening in the cyclic stress response particularly at the higher strain amplitudes of testing, which is attributed to the formation of strain-induced martensite, as confirmed by the changes in ferrite number and XRD measurements.
5. A close agreement was achieved between the numerically predicted and the experimentally obtained hysteresis loops, validating the constitutive parameters used for the analysis.

Acknowledgments

The work was carried out as a part of PhD program of the first (corresponding) author. The author thanks IGCAR management for permitting him to carryout LCF tests. The authors thank Head, FSS/MMG for the valuable suggestions during testing.

References

1. S.C.S.P. Kumar Krovvidi, G. Padmakumar, and A.K. Bhaduri, Experience of Various Materials for Design and Manufacture of Bellows for Nuclear Industry, *Adv. Mater. Proc.*, 2017, **2**(3), p 156–161
2. M. Anderson, J. Gholipour, and P. Bocher, Formability Extension of Aerospace Alloys for tube Hydroforming APPLICATIONS, *Int. J. Mater. Form.*, 2010, **3**(Suppl 1), p 303–306
3. S.C.S.P. Kumar Krovvidi and A.K. Bhaduri, Comparison between RCC-MR and ASME Section-III/NH for Creep-Fatigue Design of Bellows, *Int. J. Nucl. Energy Sci. Technol.*, 2018, **12**(4), p 331–350
4. M. Ridlova, L. Hyspecka, F. Wenger, P. Ponthiaux, J. Galland, and P. Kubecka, Strain-Induced Martensitic Transformation in Type 321 Austenitic Stainless Steel, *Journal De Physique. IV (Proceedings)*, 2003, **112**(1), p 429–432. <https://doi.org/10.1051/jp4:2003917>
5. B.R. Antoun, C. Alleman, and K.D.L. Trinidad, Experimental Investigation of Dynamic Strain Aging in 304L Stainless Steel, in *Conference Proceedings of the Society for Experimental Mechanics Series*. Springer, pp. 2019, 65–72. https://doi.org/10.1007/978-3-319-95053-2_10
6. J.A.C. Ramirez, T. Tsuta, Y. Mitani, and K. Osakada, Flow Stress and Phase Transformation Analyses in the Austenitic Stainless Steel Under Cold Working: Part 1, *Phase Transformation Characteristics and Constitutive Formulation by Energetic Criterion, JSME Int J A-SOLID M*, 2019, **35**(2), p 201–209
7. W. Li, L. Yang, C. Li, H. Chen, L. Zuo, Y. Li, J. Chen, J. He, and S. Zhang, Low-Cycle Fatigue and Fracture Behavior of Aluminized Stainless Steel AISI 321 for Solar Thermal Power Generation Systems, *Metals*, 2020, **10**(8), p 1089
8. Yu. Taran, J. Schreiber, M.R. Daymond, and E.C. Oliver, Neutron Diffraction Study of Plasticity-Induced Martensite Formation of the Austenitic Stainless Steel AISI 321, *Mater. Sci. Forum*, 2002, **404–407**, p 501–508. <https://doi.org/10.4028/www.scientific.net/msf.404-407.501>
9. M. Grosse, D. Kalkhof, M. Niffenegger, and L. Keller, Influencing Parameters on Martensite Transformation During Low Cycle Fatigue for Steel AISI 321, *Mater. Sci. Eng.-A*, 2006, **437**(1), p 109–113
10. M. Grosse, D. Kalkho, L. Keller, and N. Schell, Influence Parameters of Martensitic Transformation During Low-Cycle FATIGUE for Steel AISI 321, *Physica-B*, 2004, **350**, p 102–106
11. ASTM A240/240M-22 (2022a) Standard Specification for Chromium and Chromium-Nickel Stainless Steel Plate, Sheet, and Strip for Pressure Vessels and for General Applications, ASTM International, West Conshohocken, Pennsylvania
12. ASTM E8/8M-21 (2022b) Standard Test Methods for Tension Testing of Metallic Materials, ASTM International, West Conshohocken, Pennsylvania
13. ASTM E606/606M-21 (2021) Standard Test Method for Strain-Controlled Fatigue Testing, ASTM International, West Conshohocken, Pennsylvania
14. ASTM-E975-22 (2022c) Standard Test Method for X-Ray Determination of Retained Austenite in Steel with Near Random Crystallographic Orientation, ASTM International, West Conshohocken, Pennsylvania
15. R. Andersson, (2005) 'Deformation Characteristics of Stainless Steels', Ph.D. dissertation, Luleå University of technology, Luleå, Sweden, ISSN:1402-1544
16. RCC-MR, (2007) Design and Construction Rules for Mechanical Components of Nuclear Installations, RCC-MR, Section-1, subsection B: Class 1 Components, (2007), AFCEN, Paris
17. B.F. Langer, Design of Pressure Vessels for Low-Cycle Fatigue, *J. Basic Eng.*, 1962, **84**(3), p 389–399
18. H. Kitagawa and T. Sohmura, An X-ray Diffraction Method for Quantitative Determination of Retained Austenite in the Production Line of Metastable Austenitic Stainless Steel, *Trans. ISIJ*, 1983, **23**, p 543–549

19. S.C.S.P. Kumar Krovvidi, S. Goyal, and A.K. Bhaduri, Experimental and Numerical Investigation of High-Temperature Low-Cycle Fatigue and Creep-Fatigue Life of Bellows, *J. Mater. Eng. Perform.*, 2021, **30**(4), p 2742–2750
20. J.L. Chaboche and G. Rousselier, On the Plastic and Viscoplastic Constitutive Equations-Part II: Application of Internal Variable Concepts to the 316 Stainless Steel, *J. Press. Vessel Technol. Trans. ASME*, 1983, **105**(2), p 159–164
21. J.L. Chaboche, A Review of Some Plasticity and Viscoplasticity Constitutive Theories', *Int. J. Plast.*, 2008, **24**(10), p 1642–1693
22. R. Zauter, F. Petry, H.-J. Christ, and H. Mughrabi, Thermomechanical Fatigue Behavior of Materials, ASTM STP 1186, Ed. H. Sehitoglu, American Society for Testing and Materials, Philadelphia, 1993, pp. 70-90
23. S.S. Hecker, M.G. Stout, K.P. Staudhammer et al., Effects of Strain State and Strain Rate on Deformation-Induced Transformation in 304 Stainless Steel: Part I: Magnetic Measurements and Mechanical Behavior, *Metall. Trans. A*, 1982, **13**, p 619–626. <https://doi.org/10.1007/BF02644427>
24. D.Y. Ryoo, N. Kang, and C.Y. Kang, Effect of Ni Content on the Tensile Properties and Strain-Induced Martensite Transformation for 304 Stainless Steel, *Mater. Sci. Eng. A*, 2011, **528**(6), p 2277–2281. <https://doi.org/10.1016/j.msea.2010.12.022>
25. G. Prasad Reddy, R. Sandhya, K. Bhanu Sankara Rao, and S. Sankaran, Influence of Nitrogen Alloying on Dynamic Strain Ageing Regimes in Low Cycle Fatigue of AISI 316LN Stainless Steel, *Procedia Eng.*, 2010, **2**(1), p 2181–2188. <https://doi.org/10.1016/j.proeng.2010.03.234>
26. C. Kim, Nondestructive Evaluation of Strain-Induced Phase Transformation and Damage Accumulation in Austenitic Stainless Steel Subjected to Cyclic Loading, *Metals*, 2018, **8**, p 14. <https://doi.org/10.3390/met8010014>
27. G.V. Prasad Reddy, R. Sandhya, S. Sankaran, and M.D. Mathew, Low Cycle Fatigue Behavior of 316LN Stainless Steel Alloyed with Varying Nitrogen Content: Part I: Cyclic Deformation Behavior, *Metall. Mater. Trans. A*, 2014, **45**, p 5044–5056
28. H.-J. Christ and H. Mughrabi, Cyclic Stress-Strain Response and Microstructure Under Variable Amplitude Loading, *Fatigue Fract. Eng. Mater. Struct.*, 1996, **19**(2), p 335–348
29. S.S. Yadav, S.C. Roy, and S. Goyal, A Comprehensive Review and Analysis of Masing/Non-Masing Behavior of Materials Under Fatigue, *Fatigue Fract. Eng. Mater. Struct.*, 2023, **46**(3), p 759–783

Publisher's Note Springer Nature remains neutral with regard to jurisdictional claims in published maps and institutional affiliations.

Springer Nature or its licensor (e.g. a society or other partner) holds exclusive rights to this article under a publishing agreement with the author(s) or other rightsholder(s); author self-archiving of the accepted manuscript version of this article is solely governed by the terms of such publishing agreement and applicable law.